Supplementary information

Switching and Detection of the Néel Vector Multistate in Non-Collinear Antiferromagnetic NiF_2 for Logic Applications

Zidong Wang, Hua Xu, Boshi Mu, Yan Liu*

Zidong Wang − *College of Sciences, Northeastern University, Shenyang 110819, China;*

Email: 2310028@stu.neu.edu.cn

Hua Xu − *College of Sciences, Northeastern University, Shenyang 110819, China;* **Email:**

2010022@stu.neu.edu.cn

Boshi Mu − *College of Sciences, Northeastern University, Shenyang 110819, China;* **Email:**

2210023@stu.neu.edu.cn

Yan Liu − *College of Sciences, Northeastern University, Shenyang 110819, China;* **Email:**

liuyanphys@mail.neu.edu.cn

Contents:

Note 1. Methods

Micromagnetic Simulation of Field-Induced Spin Dynamics

In order to study the four-state switching behavior in NiF_2 under different magnetic field orientations, we have developed a micromagnetic simulation framework. The effective fields of NiF_2 body center and angular position spins are expressed as:

$$\begin{aligned}\mathbf{H}_{eff1} &= -H_{ex}\mathbf{M}_2 - 2H_{ka}M_{1a}\mathbf{n}_a + 2H_{kb}M_{1b}\mathbf{n}_{\mathrm{b}} + 2H_{kc}M_{1c}\mathbf{n}_{\mathrm{c}} + \mathbf{H} \\ \mathbf{H}_{eff_2} &= -H_{ex}\mathbf{M}_1 + 2H_{ka}M_{2a}\mathbf{n}_a - 2H_{kb}M_{2b}\mathbf{n}_{\mathrm{b}} + 2H_{kc}M_{2c}\mathbf{n}_{\mathrm{c}} + \mathbf{H}\end{aligned} \quad (1)$$

where $\mathbf{n}_a, \mathbf{n}_b, \mathbf{n}_c$ is the unit vectors in the crystal coordinate axis.

We propose a NiF_2/Pt bilayer structure as the model system. To switch the AFM magnetizations, an external magnetic field is applied within the easy plane, with its direction adjustable at any angle in the ab-plane. The dynamic behavior of the AFM

magnetizations is described by two coupled Landau-Lifshitz-Gilbert (LLG) equations:[1]

$$\begin{aligned}\frac{d\mathbf{M}_1}{dt} &= \gamma\left[\mathbf{H}_{eff1}\times\mathbf{M}_1\right]+\alpha[\mathbf{M}_1\times\frac{d\mathbf{M}_1}{dt}]\\ \frac{d\mathbf{M}_2}{dt} &= \gamma\left[\mathbf{H}_{eff_2}\times\mathbf{M}_2\right]+\alpha[\mathbf{M}_2\times\frac{d\mathbf{M}_2}{dt}]\end{aligned} \quad (3)$$

where γ is the spin magnetic ratio, α is the Gilbert effective damping constant.

Additionally, we apply the fast Fourier transform (FFT) to time-dependent magnetization data to extract resonance frequencies and amplitdes, as shown in Fig. S1.

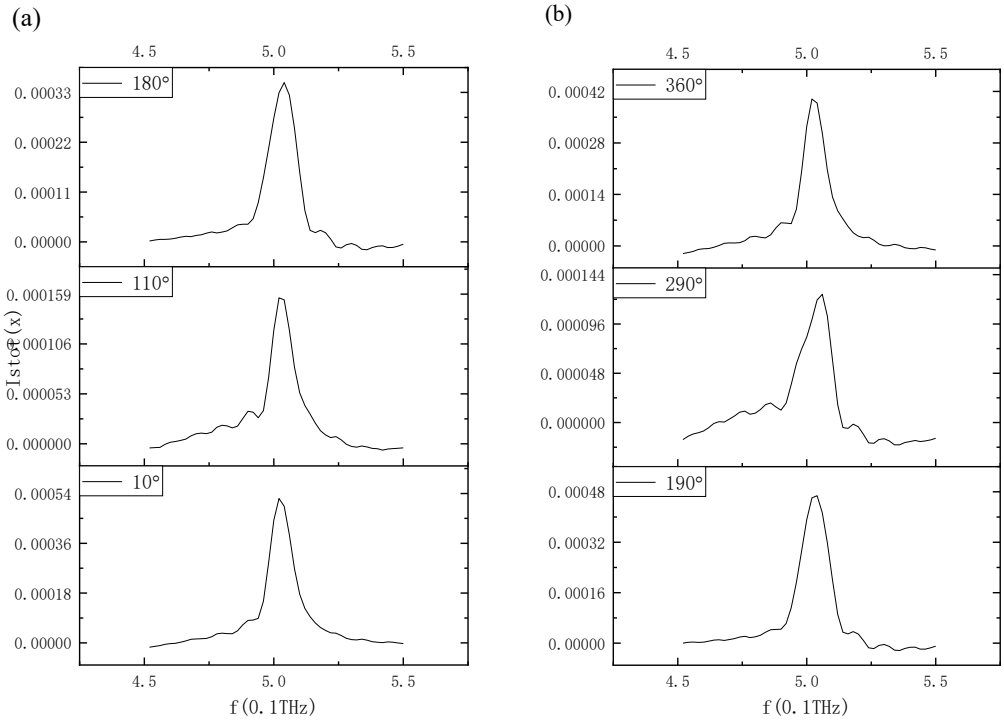

Fig. S1. (a)-(b) The fast Fourier transform (FFT) to time-dependent magnetization data to extract AFM-mode resonance frequencies at different angles of magnetic field.

Note 2. Validation of magnetic parameters via magnetization curves and resonance frequencies

A variety of parameter sets have been proposed to describe the spin interaction in NiF_2. Table SI provides a comparative summary of various parameters in a representative spin Hamiltonian, situating the parameter set employed in this work within the broader landscape of reported models.

Table SI. Representative parameter set of NiF_2 in the selected literature. Exchange parameters, easy-axis anisotropy parameters and hard-axis anisotropy parameters in the literature are given in cm^{-1}/Tesla (T). The parameter set in this work is given in Tesla (T), representing the amplitude of the effective magnetic field terms, and is highlighted in bold for comparison.

Reference	Method	H_{ex}	H_{ka}	H_{kc}	Canted angle
P. L. Richards [2]	Experiment	40T	$0.833cm^{-1}$	$2.53cm^{-1}$	
W. J. Brya *et al*. [3]	Experiment	$13.4cm^{-1}$			
P. A. Fleury *et al*. [4]	Experiment	$13.87cm^{-1}$	$1.66cm^{-1}$	$4.36cm^{-1}$	
S. Wang *et al*. [5]	Experiment		$1.66cm^{-1}$	$3.86cm^{-1}$	
S. J. Joshua *et al*. [6]	Experiment	$15.63cm^{-1}$	$1.66cm^{-1}$	$3.86cm^{-1}$	
E. Meloche *et al*. [7]	Experiment	$13.8cm^{-1}$	$1.66cm^{-1}$	$4.2cm^{-1}$	0.49°
A. Hariki *et al*. [8]	Experiment	1.47meV			
T. Moriya [9]	Experiment	$11.875cm^{-1}$	$2.67cm^{-1}$	$4.19cm^{-1}$	
A. H. Cooke *et al*. [10]	Experiment	$13.4cm^{-1}$	$1.75cm^{-1}$		0.9°
H. Shi *et al*. [11]	Experiment	$13.87cm^{-1}$			0.43°
R. G. Shulman [12]	Experiment	$95cm^{-1}$	$2.67cm^{-1}$	$4.18cm^{-1}$	1.3°
Z. Wang *et al*. [13]	**LLG**	**40T**	**6T**	**19T**	**0.5°**
This work	**LLG**	**40T**	**6T**	**19T**	**0.5°**

The comparison in Table SI further illustrates that in micromagnetism simulations, all parameters represent effective fields in T, whereas most experiment studies employ cm^{-1} units. This unit conversion does not compromise the physical consistency of the model, as the relevant physical phenomena are determined by relative ratios of interaction strengths (e.g., $|H_{ex}/H_{ka}|$), which remain consistent with the parameter sets

obtained from spectral data fitting. Among the parameters reported in the literature, the ratio of the exchange constant to the hard-axis anisotropy constant to the easy-axis anisotropy constant is approximately 60:25:8. Based on this ratio, the current parameter set was selected for its ability to simultaneously reproduce three key experimental benchmarks: the spin orientation tilt angle of approximately 0.5° at zero magnetic field; the critical transition field of approximately 7T observed when a magnetic field is applied along the [100] direction; and the two characteristic frequencies of magnetically resonantly excited spins at zero field. The comprehensive fulfillment of these static and dynamic constraints ensures that the selected parameters reliably characterize the core magnetic field-angle dependence behavior investigated in this study.

About saturation magnetization: In this study, the saturation magnetization was set to 2.79×10^4A/m. This value is calculated by the saturation magnetization formula ($M_s = Ng_j J\mu_B$) based on the NiF_2-related magnetic parameters obtained from previous widely recognized experimental investigations. The specific analysis is as follows. According to the NiF_2 rutile lattice parameters (a=b= 4.651Å), (c= 3.084Å) reported by Borovik-Romanov *et al.* [14], each unit cell contains two Ni atoms, and the unit cell volume ($V_{cell} \approx 67.9\times10^{-24}cm^3$). Therefore, the number of Ni atoms per unit volume $N = \frac{2}{V_{cell}} \approx 2.945\times10^{28} m^{-3}$. According to the experimental results of Richards [2] on the magnetic resonance of NiF_2, the Lande factor g_j of NiF_2 is $g_j \approx 2.57$. Combined with the Raman scattering study of NiF_2 by Meloche *et al.* [7], NiF_2 corresponds to the total angular momentum quantum number $J = 4$. The above

parameters are substituted into the saturation magnetization formula $M_s = Ng_j J\mu_B \approx 2.79\times10^4 A/m$.

About damping coefficient: We note that the literature directly reporting the damping coefficient of NiF_2 Gilbert is scarce, and only our team's previous research mentions this parameter [13]. Here we derive two dimensions from the isomorphic material analogy and theoretical model, and explain the selection logic of α= 0.0035 in detail to prove its physical rationality:

(a) NiF_2 is rutile structure (space group $P4_2/mnm$), and its magnetic interaction is dominated by 'Heisenberg exchange and single-ion anisotropy', which has common magnetic damping mechanisms with rutile AFMs (such as FeF_2) and weak ferromagnetic (such as α-Fe_2O_3) with the same structure, and the main intrinsic damping sources are spin-lattice coupling and magnetic domain scattering. The range of Gilbert damping coefficient of this kind of material has been clear: FeF_2 (rutile AFM, which belongs to transition metal fluoride with NiF_2), and its intrinsic damping $\alpha \approx 2\times10^{-3} \sim 4\times10^{-3}$ is reported in the literature [15]. Weak ferromagnetic insulators (such as α-Fe_2O_3): The damping coefficients reported in the literature are concentrated in $\alpha \approx 2.5\times10^{-3} \sim 5\times10^{-3}$ [16]. It can be seen that as a material with the same structure and the same magnetic mechanism, the damping coefficient of NiF_2 should naturally fall in the $\alpha \approx 2\times10^{-3} \sim 5\times10^{-3}$ interval, and the $\alpha \approx 0.0035$ we selected is at the center of this range, which conforms to the common law of material magnetic damping.

(b) Theoretical model derivation: Even in the absence of direct measurement data, we can invert the reasonable damping range by combining the magnetic parameters

identified by NiF_2 with the correlation model of Gilbert damping and magnetic interaction. Previous studies have shown that the intrinsic Gilbert damping is only determined by the magnetic moment relaxation of the AFM itself, the formula is [17]: $\alpha = \frac{\Delta w_0}{w_{ex}}$, where Δw_0 corresponds to the angular frequency of the intrinsic resonance line width. Richards reported that the magnetic resonance linewidth of NiF_2 is $0.56cm^{-1}$ [2]. $w_{ex} = 2\pi\gamma H_{ex}$ is the exchange angular frequency. Calculated: $\alpha = \frac{\Delta w_0}{w_{ex}} = \frac{2\pi\nu(c/n)}{2\pi\gamma H_{ex}} = \frac{2\times 3.1416\times 0.56\times(3\times 10^{10}/1.38) rad/s}{2\times 3.1416\times 1.6672\times 10^{11}\times 40 rad/s} \approx 0.0035$. The theoretical inversion results are in good agreement with our selected α = 0.0035, which proves that the parameter selection is based on the quantitative derivation of the nature of magnetic interaction.

In summary, the basis for our selection α = 0.0035 is based on the dual logic of 'common law of isomorphic materials and theoretical derivation of magnetic interaction'.

To validate the magnetic parameters used in our simulations, we compared our results with experimental data reported in references, as shown in Fig. S2.

(a) Magnetization curve of NiF_2:

Under an external magnetic field applied along the [100] direction, the magnetization increases monotonically as the field rises (Fig. S2(a)).

The slope extracted from our simulated magnetization curve is:

$$k = \frac{(0.7980 - 0.016)\ \mu_B \text{ per Ni atom}}{(60 - 1.2)\ \text{T}} \approx 1.33\times 10^{-2}\ \mu_B \text{ per Ni atom/T}$$

The slope reported in the experimental data is [8]:

$$k = \frac{(0.038 - 0.03)\ \text{Bohr magnetons}}{(6 - 0)\ \text{kilogauss}} \approx 1.33 \times 10^{-3}\ \text{Bohr magnetons/kilogauss}$$

Since each NiF_2 formula unit contains 1 Ni atoms, the slope conversion is as follows:

$$k = 1.33 \times 10^{-3} \times \frac{1\mu_B}{\text{Bohr magnetons}} \times \frac{1\text{Bohr magnetons}}{\text{Ni atom}} \times \frac{1\text{kilogauss}}{0.1\text{T}}$$
$$\approx 1.33 \times 10^{-2}\ \mu_B\ \text{per Ni atom/T}$$

The above analysis shows that the simulated slope is in excellent agreement with the experimental slope reported in [8].

(b) Two intrinsic resonance modes of NiF_2:

Under an external magnetic field applied along the [100] direction, the non-collinear spin structure of NiF_2 gives rise to a small net magnetization, which exhibits oscillations that depend on the field strength. This oscillatory behavior corresponds to a FM-mode. In addition, NiF_2 also possesses an intrinsic AFM-mode, which is more stable and oscillates at a higher frequency than the FM-mode, as shown in Fig. S2(b).

The slope of the FM-mode in our simulation:

$$k = \frac{(2.2 - 0.8) \times 0.1\text{THz}}{(5 - 0.3)\ \text{T}} \approx 0.03\,\text{THz/T}$$

The slope reported in the experimental data is:

$$k = \frac{(9 - 4)\ \text{cm}^{-1}}{(50 - 0)\ \text{kOe}^{-1}} = 0.1\text{cm}^{-1}\text{kOe}^{-1}$$

After conversion:

$$k = 0.1\text{cm}^{-1}\text{kOe}^{-1} = 0.1 \times (30\text{GHz}) \times \frac{1}{0.1\ \text{T}} = 0.1 \times 30\text{GHz} \times \frac{10}{\text{T}} = 0.03\,\text{THz/T}$$

The slope of the FM-mode is about 0.03THz/T, in close agreement with the reported value of 0.03THz/T in Refs. [2,3,14]. In addition, the slope of the AFM mode is remains nearly constant, also consistent with the experimental given in Refs. [2,6,14].

It is worth noting that the parameter set used here has been validated in a different context within our research group. As reported in Ref. [13], these parameters proved effective in simulating the THz-frequency dynamics of NiF_2 for spintronic applications, providing additional support for their appropriateness in modeling the system's magnetic behavior.

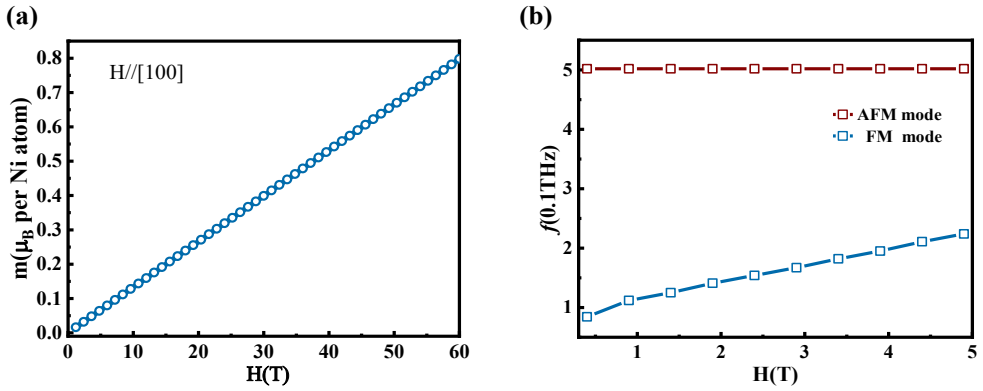

Fig. S2. (a) Magnetization evolution of NiF_2 under an external magnetic field along the [100] (*a*-axis) direction. (b) The dependence of the two spin-eigenfrequency oscillation frequencies of NiF_2 on the external magnetic field.

(c) Summary:

The simulation results exhibit excellent agreement with experimental data in both magnetization curves and intrinsic oscillation frequencies, strongly validating the effectiveness of the selected magnetic parameters.

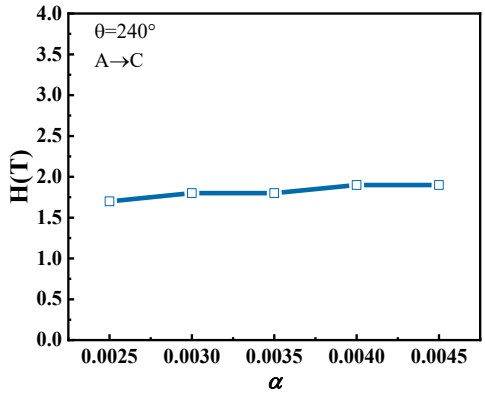

Fig. S3. The threshold magnetic field strength varies with the damping coefficient.

In addition, we evaluated the effect of damping constant on the threshold field strength through a series of simulations. As shown in Fig. S3, in the range of 0.0025 to 0.0045, the threshold magnetic field strength only shows a slight fluctuation with the increase of α. This indicates that the kinetic phenomena reported in this study are not sensitive to the specific value of α within this reasonable range. Therefore, the use of α = 0.0035 will not essentially affect the validity of the research conclusions.

Note 3. The 180° and 90° switching dynamics of Néel vector

Studying the dynamics of the four-state switching behavior is crucial for understanding microscopic mechanisms and enabling applications [18]. Below, we explore the dynamic properties of magnetic moments in four-state switching. Fig. S4(a) depicts the 90° switching of the Néel vector triggered by an external magnetic field, where θ=230° for switching from state A to C (A→C) and θ=170° for switching from state A to B (A→B) a θ=45° for switching from state B to D (B→D).

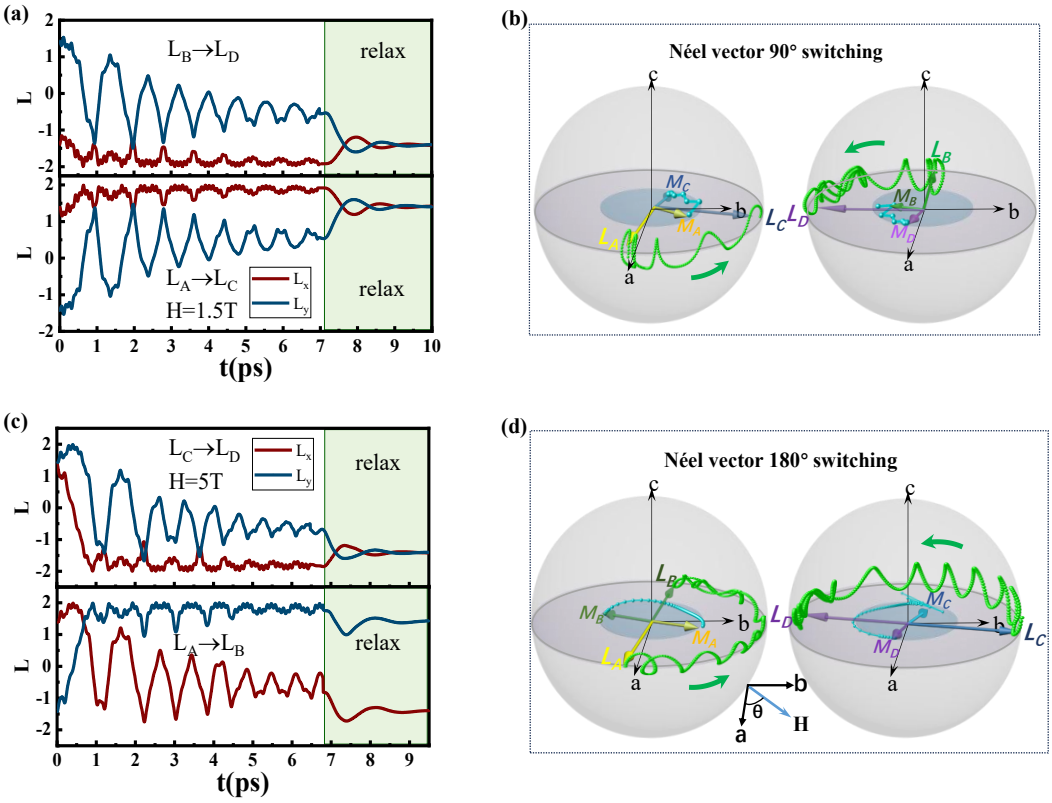

Fig. S4. (a) The magnetization dynamics of the 90° switching of Néel vector, which is a representation of the switching of Néel vector from A to C and B to D, where the *x* and *y* component of the Néel vector as a function of time is shown. The magnetic field is applied from 0-7 ns, and it is turned off at 7ns. (b) The trajectories of the Néel vector and the FM vector during the 90° switching corresponding to Fig. S1(a). (c) The magnetization dynamics of the 180° switching of Néel vector, which illustrates the temporal evolution of the Néel vector's *x* and *y* components during its switching transitions between states A to B and C to D. The applied magnetic field, active during the 0-6.8 ns timeframe, was terminated precisely at t=6.8 ns. (d) The trajectories of the Néel vector and FM vector during the 180° switching corresponding to Fig. S1 (c).

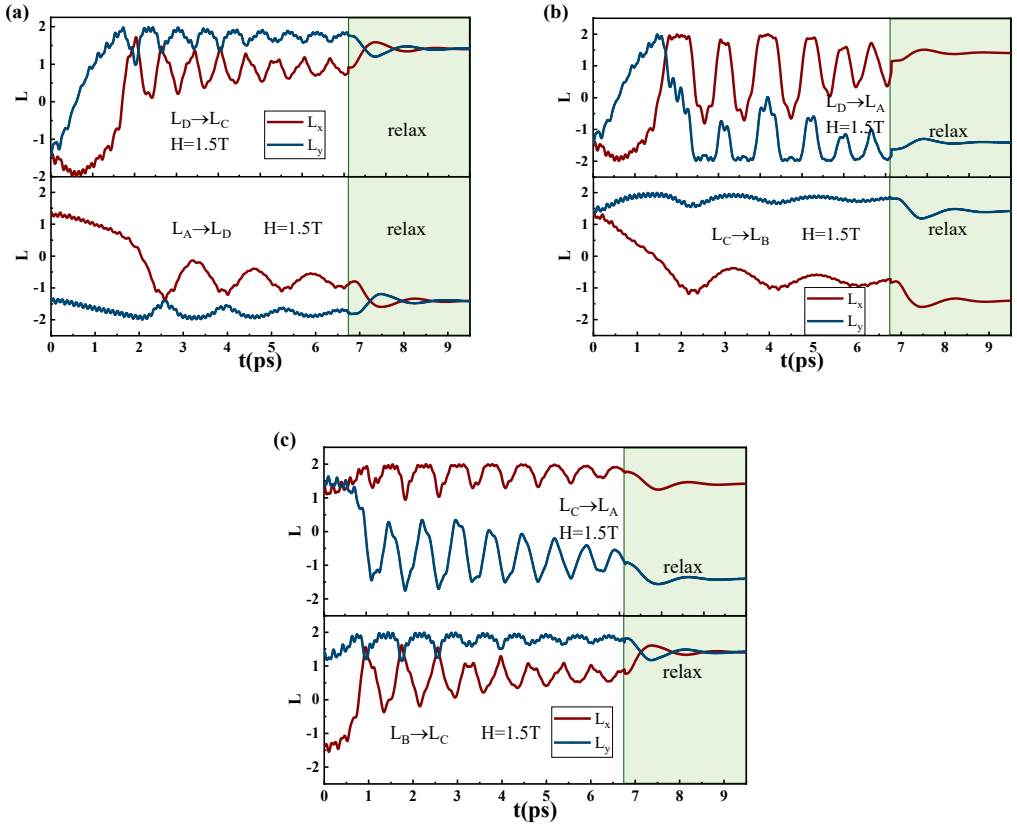

Fig. S5. (a)- (c) The magnetization dynamics of the 90° and 180° switching of Néel vector, The magnetic field is applied from 0-7 ns, and it is turned off at 7ns.

Fig. S4(b) provides a comprehensive visualization of the 90° switching mechanism. Each trajectory depicted on the unit sphere is correlated with **L** and **M**, providing an intricate representation of the underlying processes governing the magnetization dynamics and the reorientation behavior of the Néel vector under varied magnetic field conditions. Fig. S4(c) presents the 180° switching process, where θ =170° for switching from state A to B (A→B) and θ =15° for switching from state D to C (D→C). Following a 1.5ps delay, **L** begins to reorient along the *ab*-plane and the magnetization sublattices reach a stable oscillation state in the opposite direction. Finally, after removing the external magnetic field, the 180° magnetization switching is stabilized in a nearby equilibrium state. The 180° magnetization reversal trajectory

of magnetization vectors **L** and **M** is described in Fig. S4(d). The four states can be switching among each other, and the other dynamic behaviors of the Néel vector switching are shown in Figs. S5(a)-(c).

Note 4. The switching time of Néel vector

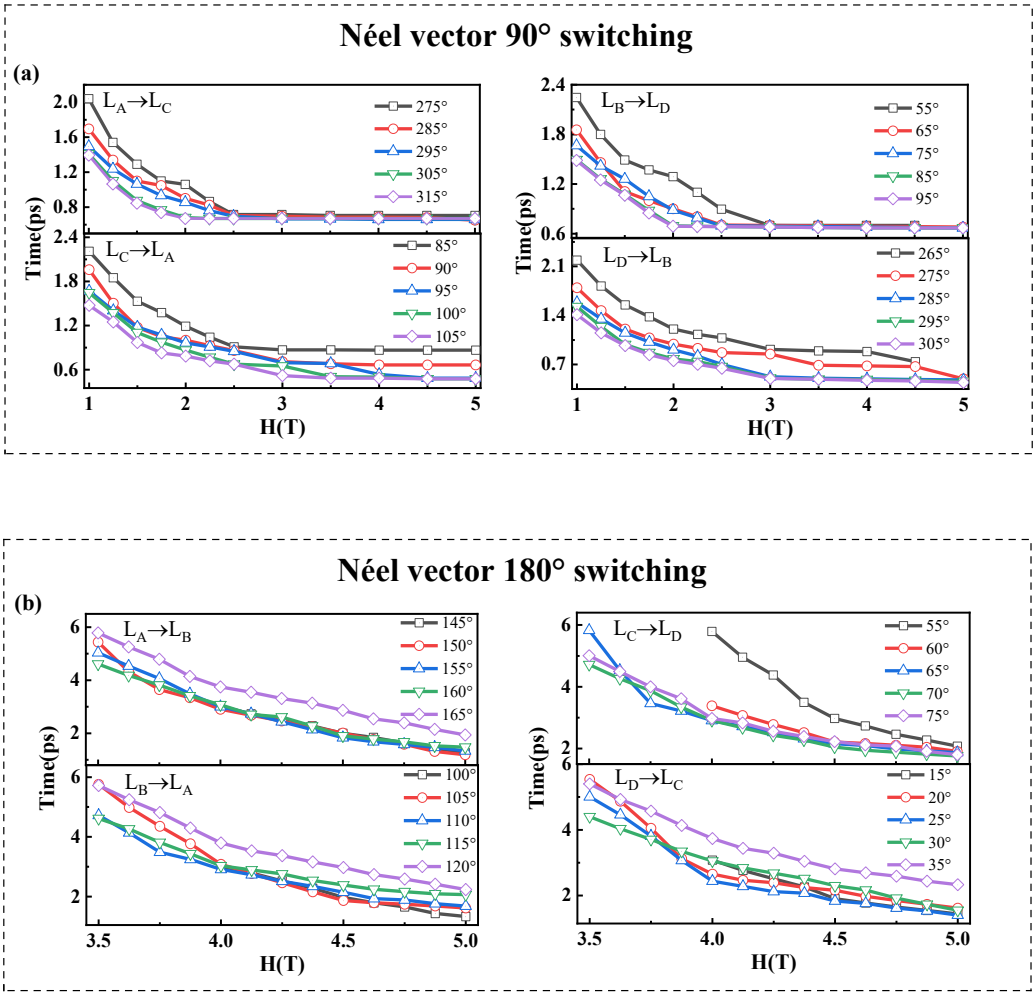

Fig. S6. (a) The switching time as a function of the magnetic field for the 90° switching of Néel vector when the magnetic field is applied in different directions. (b) The switching time of the 180° switching of Néel vector displays a dependence on the direction of the applied magnetic field.

The 'switching time' is defined as the transition period from the initial state to the

new steady state. Ultimately, the sublattice magnetization relaxes to the new steady state, completing the magnetization reversal process. Figure S4 shows the switching time under various magnetic fields. The 90° switching of the Néel vector can achieve ultrafast magnetization reversal within 0.5 ps, as shown in Fig. S6 (a). The capability to achieve such ultrafast switching of Néel vector opens up new possibilities for the application of NiF_2 in advanced technologies. Ultrafast magnetization switching has been reported in many references.

Similarly, the 180° switching time for Néel vector also decreases with increasing magnetic field, as shown in Figs. S6 (b). It is observed that at a critical magnetic field of 3.5T, the 180° switching time for Néel vector is approximately 4-6 ps. As the magnetic field increases, the switching time decreases, reaching about 1.5 ps at magnetic fields of 5T. However, previous studies have yet to uncover mechanisms capable of achieving controllable switching between multiple magnetization vector states within a material, particularly in AFM systems. The strong coupling between sublattice magnetizations and their weak response to external stimuli pose significant challenges for realizing multi-state magnetization vector switching. Our findings introduce NiF_2 as a promising material for AFM spintronics, offering novel opportunities for ultra-fast magnetic switching applications.

Note 5. Advantages of NiF_2 four-state switching

Building on the demonstrated four-state operation, we systematically validate the inherent advantages of NiF_2 by comparing it with other representative AFM systems (Mn_3Sn, Mn_5Si_3, FeRh, Fe_2O_3) in Table SII.

As shown in Table SII, the Néel vector switching in previous typical AFM systems was limited to a single switching type: Mn_3Sn could achieve 60° or 180° reversal and Mn_5Si_3 could only achieve 180° reversal, corresponding to two- or three-state storage; FeRh supported 90° rotation due to phase transitions, while Fe_2O_3 enabled 60° switching via its three easy axes, corresponding to three-state storage.

Table SII. Comparison of Néel vector switching characteristics and multi-state storage potential of typical AFM systems

Material	Storage state attributes	Number of storage states	Intrinsic symmetry basis	Switching type
Mn_3Sn [19,22]	Intrinsic steady state	2-3 states	Uniaxial kagome lattice	60° or 180° switching
Mn_5Si_3 [20]	Intrinsic steady state	2 states	Uniaxial easy axis	180° switching
FeRh [21]	Phase transition induced steady state	2 states	Uniaxial easy axis	90° switching
α-Fe_2O_3 [16]	Intrinsic steady state	3 states	Three-axis hexagonal lattice	60° switching
NiF_2(This work)	**Intrinsic steady state**	**4 states**	**Two-axis positive trading axis**	**90° and 180° switching**

In contrast, NiF_2 leverages its intrinsic biaxial magnetic anisotropy and four fundamental intrinsic states to simultaneously enable both 90° rotation and 180° reversal of the Néel vector: The 90° rotation enables state switching between adjacent easy axes, while the 180° reversal facilitates state transition to the opposite axis. Together, they support encoding across four stable states, overcoming the limitations

of traditional AFM's single switching mode. Compared to binary systems, quaternary logic requires only half the number of digits to represent the same information, reducing memory elements by 50%. A key advantage of quaternary logic is its native compatibility with binary systems, as its four states map directly onto two binary bits. Relative to ternary logic, quaternary representation uses fewer digits and offers a ~21% reduction in memory elements for the same information capacity. Implementing ternary logic would require a complete and costly redesign of the existing binary-based computing architecture. In contrast, quaternary logic can be integrated seamlessly with current binary infrastructure, significantly lowering development costs. Furthermore, the NiF_2 four-state signal discrimination exceeds 30%, simultaneously enhancing encoding dimensions while ensuring stability and reliability for practical storage. This provides crucial material and physical support for high-density multi-level AFM memory devices.

Note 6. The dependence of the amplitude of the magnetized sublattice oscillation on the angle of the external magnetic field

The resonance amplitude of AFM mode shows good regularity in the direction of external field, as shown in Fig.S7 (a). However, the amplitude of the spin current of the FM mode as an external field is jagged, and it is difficult to distinguish the four states, as shown in Figure S7 (b). In addition, when the external magnetic field deflects 10° to the *ab* plane in the *z*-direction, the resonance amplitude of the AFM mode is almost unaffected, as shown in Figure S7 (c). But the FM mode is greatly affected by the angle, as shown in Figure S7 (d). Consequently, the AFM mode demonstrates superior stability compared to the FM mode.

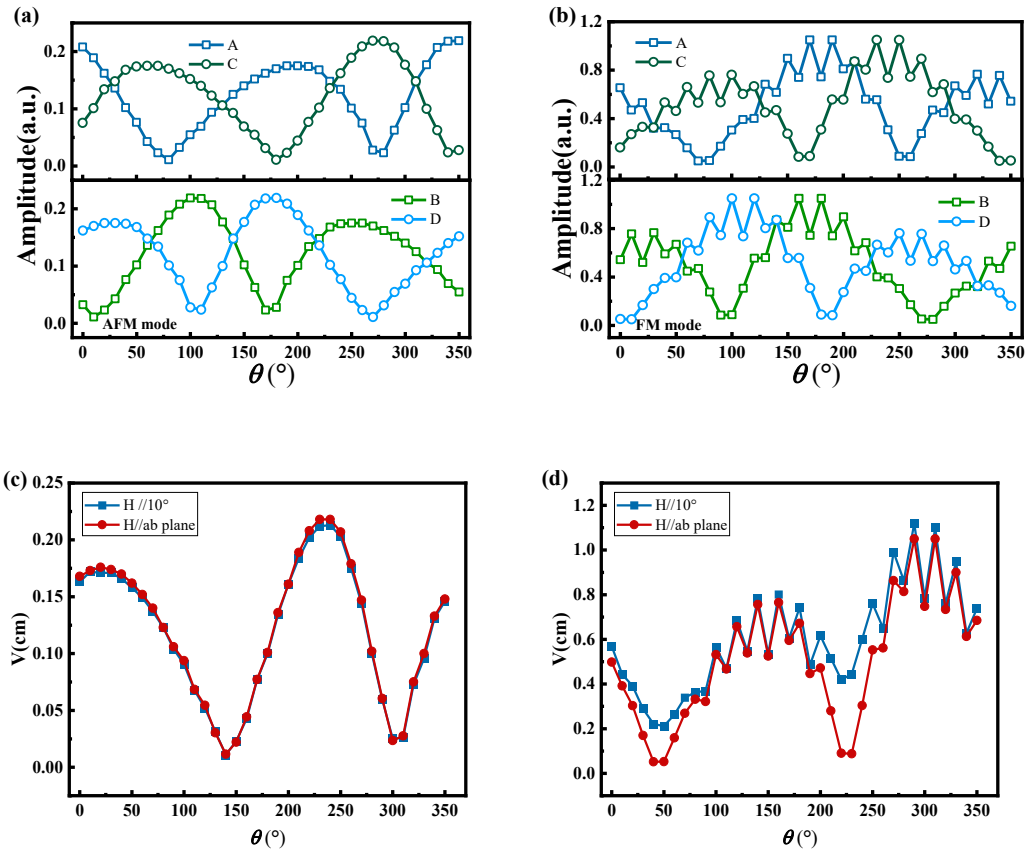

Fig. S7. (a) The dependence of the oscillation amplitude of AFM mode on the angle of magnetic field for the four states. (b) The dependence of the oscillation amplitude of FM mode on the angle of magnetic field for the four states. (c) The dependence of the oscillation amplitude of the AFM mode on the angle between the magnetic field and the ab plane. (d) The dependence of the oscillation amplitude of the FM mode on the angle between the magnetic field and the *ab*-plane.

Note 7. The output charge current in the Pt layer under different initial states as a function of linearly polarized THz microwave field angles

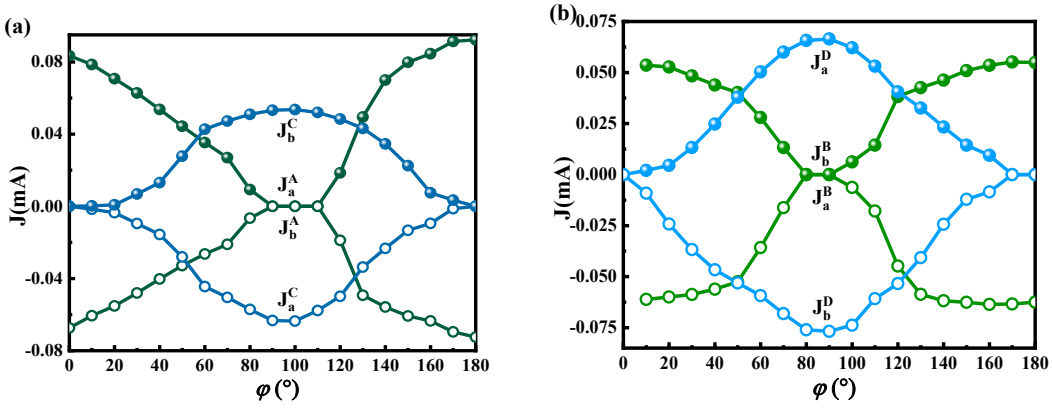

Fig. S8. (a)-(b) The output charge current in the Pt layer under different initial states as a function of linearly polarized THz microwave field angles. Where φ represents the angle between the THz microwave fields and the *a*-axis.

Similar to the circularly polarized case, the charge currents can also be excited by the linearly polarized THz microwave field. The J_a or J_b induced in the HM layer induced by the linearly polarized THz excitation are shown in Figs. S8 (a) and S8(b). The angle that distinguishes the four magnetization states is identical to that of the circularly polarized THz field. However, the output current density is relatively small, approximately 50% of that observed in the circular polarization case.

In addition, we considered the effect of clockwise and counterclockwise rotating circularly polarized microwave fields on the excitation of AFM mode. We found that, regardless of whether the circularly polarized microwave field rotates clockwise or counterclockwise, it has no effect on the excitation of AFM mode, as shown in Fig. S9.

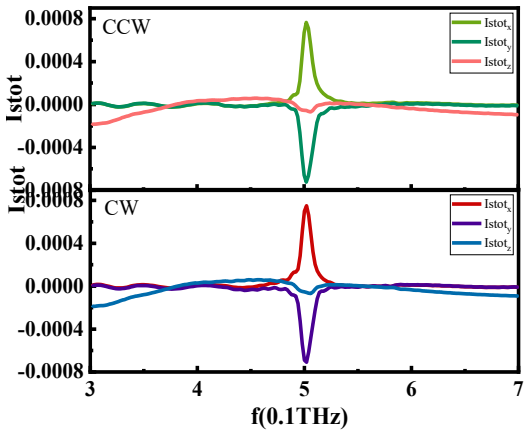

Fig. S9. The effect of clockwise and counterclockwise rotating circularly polarized microwave fields on the excitation of AFM mode.

REFERENCES

[1] O. S. Temnaya, A. R. Safin, D. V. Kalyabin, S. A. Nikitov, *Phys. Rev. Appl.* 2022, **18**, 014003.

[2] P. L. Richards, *J. Appl. Phys.*, 1963, **34**, 1237–1238.

[3] W. J. Brya and Peter M. Richards, *AIP Conf. Proc.*, 1973, **10**, 729.

[4] P. A. Fleury, R. Loudon and L. R. Walker, *J. Appl. Phys.*, 1971, **42**, 1649-1650.

[5] S. Wang, X. Kuang, M. Duan and C. Zhang, *Phys. Status Solidi B*, 2010, **247**, 416-421.

[6] S. J. Joshua and A. P. Cracknell, *J. Phys. C: Solid State Phys.*, 1969, **2**, 24.

[7] E. Meloche, M. G. Cottam, V. P. Gnezdilov and D. J. Lockwood, *Phys. Rev. B*, 2010, **81**, 024426.

[8] A. Hariki, K. Sakurai, T. Okauchi and J. Kuneš, *npj Quantum Mater.*, 2025, **10**, 49.

[9] T. Moriya, *Phys. Rev.*, 1960, **117**, 635.

[10] A. H. Cooke, K. A. Gehring and R. Lazenby, *Proc. Phys. Soc.*, 1965, **85**, 967.

[11] H. Shi and D. Lederman, *Phys. Rev. B*, 2004, **69**, 214416.

[12] R. G. Shulman, *Phys. Rev.*, 1961, **121**, 125.

[13] Z. Wang, H. Xu, X. Shen and Y. Liu, *J. Phys. D: Appl. Phys.*, 2024, **57**, 165004.

[14] A. S. Borovik-Romanov, A. N. Bazhan and N. M. Kines, *Zh. Eksp. Teor. Fiz.*, 1973, **64**, 1367-1382.

[15] D. J. Lockwood, Low Temp. Phys., 2007, 33, 749-762.

[16] Y. Cheng, S. Yu, M. Zhu, J. Hwang and F. Yang, *Phys. Rev. Lett.*, 2020, **124**, 027202.

[17] R. Khymyn, I. Lisenkov, V. Tiberkevich, B. A. Ivanov and A. Slavin, *Sci. Rep.*, 2017, **7**, 43075.

[18] C. Grezes, B. Julsgaard, Y. Kubo, W. L. Ma, M. Stern, A. Bienfait, K. Nakamura, J. Isoya, S. Onoda, T. Ohshima, V. Jacques, D. Vion, D. Esteve, R. B. Liu, K.

Molmer, P. Bertet, *Phys. Rev. A* 2015, **92**, 020301.

[19] T. Higo, K. Kondou, T. Nomoto, M. Shiga, S. Sakamoto, X. Chen, D. Nishio-Hamane, R. Arita, Y. Otani, S. Miwa and S. Nakatsuji, *Nature*, 2022, **607**, 474–479.

[20] L. Han, X. Fu, R. Peng, X. Cheng, J. Dai, L. Liu, L. Li, Y. Zhang, W. Zhu, H. Bai, Y. Zhou, S. Liang, C. Chen, Q. Wang, X. Chen, L. Yang, Y. Zhang, C. Song, J. Liu and F. Pan, *Sci. Adv.*, 2024, **10**, eadn0479.

[21] H. Wu, H. Zhang, B. Wang, F. Groß, C. Y. Yang, G. Li, C. Guo, H. He, K. Wong, D. Wu, X. Han, C. Lai, J. Grafe, R. Cheng and K. L. Wang, *Nat. Comm.*, 2022, **13**, 15434.

[22] G. K. Krishnaswamy, G. Sala, Benjamin Jacot, Charles-Henri Lambert, Richard Schlitz, Marta D. Rossell, Paul Nöel, and Pietro Gambardella, *Phys. Rev. Appl.*, 2022, **18**, 024064.